

# S-PLUS DR1 galaxy clusters and groups catalogue using PzWav

S. V. Werner<sup>1,2\*</sup>, E. S. Cypriano<sup>2</sup>, A. H. Gonzalez<sup>3</sup>, C. Mendes de Oliveira<sup>2</sup>,  
 P. Araya-Araya<sup>2</sup>, L. Doubrawa<sup>2</sup>, R. Lopes de Oliveira<sup>2,5,6</sup>, P. A. A. Lopes<sup>4</sup>,  
 A. Z. Vitorelli<sup>2,10</sup>, D. Brambila<sup>4</sup>, M. Costa-Duarte<sup>2</sup>, E. Telles<sup>6</sup>, A. Kanaan<sup>7</sup>, T. Ribeiro<sup>8</sup>,  
 W. Schoenell<sup>9</sup>, T. S. Gonçalves<sup>4</sup>, K. Menéndez-Delmestre<sup>4</sup>, C. R. Bom<sup>11,12</sup>,  
 L. Nakazono<sup>2</sup>

<sup>1</sup>*School of Physics and Astronomy, University of Nottingham, Nottingham, NG7 2RD, UK*

<sup>2</sup>*Departamento de Astronomia, Instituto de Astronomia, Geofísica e Ciências Atmosféricas da USP, Cidade Universitária, 05508-900, São Paulo, SP, Brazil*

<sup>3</sup>*Department of Astronomy, University of Florida, 211, Bryant Space Center, Gainesville, FL 32611, USA*

<sup>4</sup>*Observatório do Valongo, Universidade Federal do Rio de Janeiro, Ladeira Pedro Antônio 43, Rio de Janeiro, RJ 20080-090, Brazil*

<sup>5</sup>*Departamento de Física, Universidade Federal de Sergipe, Av. Marechal Rondon, S/N, 49100-000 São Cristóvão, SE, Brazil*

<sup>6</sup>*Observatório Nacional, Rua General José Cristino, 77, São Cristóvão, 20921-400, Rio de Janeiro, RJ, Brazil*

<sup>7</sup>*Departamento de Física, Universidade Federal de Santa Catarina, Florianópolis, SC, 88040-900, Brazil*

<sup>8</sup>*NOAO, 950 North Cherry Ave. Tucson, AZ 85719, United States*

<sup>9</sup>*GMTO Corporation, N. Halstead Street 465, Suite 250, Pasadena, CA 91107, United States*

<sup>10</sup>*AIM, CEA, CNRS, Université Paris-Saclay, Université de Paris, F-91191 Gif-sur-Yvette, France*

<sup>11</sup>*Centro Brasileiro de Pesquisas Físicas, Rua Dr. Xavier Sigaud 150, CEP 22290-180, Rio de Janeiro, RJ, Brazil*

<sup>12</sup>*Centro Federal de Educação Tecnológica Celso Suckow da Fonseca, Rodovia Mário Covas, lote J2, quadra J, CEP 23810-000, Itaguaí, RJ, Brazil*

Accepted XXX. Received YYY; in original form ZZZ

## ABSTRACT

We present a catalogue of 4499 groups and clusters of galaxies from the first data release of the multi-filter (5 broad, 7 narrow) Southern Photometric Local Universe Survey (S-PLUS). These groups and clusters are distributed over 273 deg<sup>2</sup> in the Stripe 82 region. They are found using the PzWav algorithm, which identifies peaks in galaxy density maps that have been smoothed by a cluster scale difference-of-Gaussians kernel to isolate clusters and groups. Using a simulation-based mock catalogue, we estimate the purity and completeness of cluster detections: at  $S/N > 3.3$  we define a catalogue that is 80% pure and complete in the redshift range  $0.1 < z < 0.4$ , for clusters with  $M_{200} > 10^{14} M_{\odot}$ . We also assessed the accuracy of the catalogue in terms of central positions and redshifts, finding scatter of  $\sigma_R = 12$  kpc and  $\sigma_z = 8.8 \times 10^{-3}$ , respectively. Moreover, less than 1% of the sample suffers from fragmentation or overmerging. The S-PLUS cluster catalogue recovers  $\sim 80\%$  of all known X-ray and Sunyaev-Zel’dovich selected clusters in this field. This fraction is very close to the estimated completeness, thus validating the mock data analysis and paving an efficient way to find new groups and clusters of galaxies using data from the ongoing S-PLUS project. When complete, S-PLUS will have surveyed 9300 deg<sup>2</sup> of the sky, representing the widest uninterrupted areas with narrow-through-broad multi-band photometry for cluster follow-up studies.

**Key words:** galaxies: clusters: general – catalogues – surveys – cosmology: large scale structure

## 1 INTRODUCTION

Galaxy clusters are objects of keen interest in both astrophysics and cosmology. Their rather extreme environment, with a high density of galaxies and a hot and dense intracluster medium (ICM), has been established to be a driver for the apparent differential and rapid

\* E-mail: stephane.werner@nottingham.ac.uk

evolution observed in cluster galaxies, compared to field populations (e.g. Dressler 1984; Balogh et al. 1999; Poggianti et al. 1999; Peng et al. 2010; Wetzel et al. 2013).

Clusters, occupying the high-mass end of gravitationally-bound structures, are important tools to probe the process of structure formation in the Universe. The abundance and distribution of clusters are very sensitive to the density of the Universe constituents (e.g., matter, dark energy, neutrinos) as well as the degree of inhomogeneity of the matter distribution in the Universe (e.g. Allen et al. 2011; Kravtsov & Borgani 2012). Clusters are ideal to study the effect of the complex baryon physics – such as the AGN energy feedback to the ICM – (e.g. McNamara & Nulsen 2007; Böhringer & Werner 2010; Bykov et al. 2015) as well as properties of the dark matter through its mass profile (e.g. Okabe et al. 2013; Merten et al. 2015; Cibirka et al. 2017) and in colliding systems (e.g. Markevitch et al. 2004; Merten et al. 2011; Monteiro-Oliveira et al. 2017).

Due to the range and relevance of the scientific questions that the study of clusters can answer, it is paramount to have reliable and unbiased catalogues of those objects spanning over a wide range in mass. In this work, we tackle this task by using the optical detection technique PzWav (Gonzalez 2014; Euclid Collaboration et al. 2019) over the Southern Photometric Local Universe Survey (S-PLUS, Mendes de Oliveira et al. 2019) survey data.

There is a wealth of optical imaging cluster detection methods that, for a given cluster, target its member galaxies to detect the structures (e.g. Gal 2008). The main challenge faced is to disentangle real gravitationally bound galaxy cluster members from fluctuations of the observed galaxy density field. Given that the projected position of a galaxy in the sky is much more precisely determined than its radial distance, line-of-sight superpositions of uncollapsed large scale structures are a particularly relevant source of the noise. In this paper, we use the high-quality S-PLUS photometric redshifts (photo- $z$ 's) to get around this problem (Sec. 2).

The optical and near-infrared imaging cluster detection methods can be loosely split into three categories: matched filter (e.g. Postman et al. 1996; Bellagamba et al. 2017), red-sequence based (e.g. Rykoff et al. 2014; Rykoff et al. 2016) and geometrical (e.g. Couch et al. 1991; Ramella et al. 2002; Lopes et al. 2004), whereas PzWav belongs to the last category. The matched filter technique uses a priori definition of the cluster model to enhance the contrast of the cluster with the distribution of foreground and background galaxies (Postman et al. 1996). However, it is necessary to consider a luminosity function and a radial profile to build the filter. Other algorithms were created based on this technique but using different model assumptions (e.g. Kepner et al. 1999; Milkeraitis et al. 2010; Ascaso et al. 2011; Bellagamba et al. 2017). The red-sequence technique uses the assumption that clusters of galaxies have a population of red galaxies, and it searches for an excess of red galaxies compared to the field (Koester et al. 2007; Rykoff et al. 2014; Rykoff et al. 2016). The geometrical methods estimate the overdensity of galaxies in different regions and assume that clusters of galaxies are the densest regions.

The geometrical methods try to use as little prior information as possible on the nature of clusters, identifying them only as significant overdensities in the 2D projected space, preferably including some distance information. Well known implementations of this concept are the *Voroi Tesselation Method* (Ramella et al. 2001; Kim et al. 2002; Lopes et al. 2004), the *Counts in Cells Method* (Couch et al. 1991; Lidman & Peterson 1996), *Adaptive Kernel Method* (Gal et al. 2000, 2003), the *Percolation Algorithms* (Dalton et al. 1997) and the *Friends-of-friends Algorithm* (Ramella et al. 2002; van Breukelen & Clewley 2009).

The motivation for geometrical methods lies in their generality. Methods that rely more heavily on previous knowledge of cluster properties are highly sensitive to objects following the main trends, and supposedly less to the systems that lie on the fringes. Important examples are merging/multimodal clusters (e.g. Tempel et al. 2017), clusters with unusual galaxy populations (e.g. Hashimoto et al. 2019) and objects such as fossils clusters, with peculiarities in the luminosity function (e.g. Cypriano et al. 2006; Mendes de Oliveira et al. 2006). In an effort to determine the unbiased distribution of cluster features, the sample selection must be as free of priors as possible. One compelling feature of PzWav is its capacity to deal with full photometric redshift probability distribution functions,  $P(z)$ 's, such as those produced by S-PLUS.

The outline of the paper is as follows. In Section 2 we describe the first release of S-PLUS data (DR1) and the mock lightcones we used in this work. Details about the PzWav technique are given in Section 3. In Section 4 we apply PzWav over a mock catalogue. Among other tests, we find the threshold signal-to-noise ratio that yields the best compromise between purity and completeness. In Section 5 we apply the method to S-PLUS data, present the cluster catalogue, and compare it with results in the literature using observations in the same area. In Section 6, we discuss and summarise our results. We provide the full catalogue on GitHub<sup>1</sup>. We use a  $\Lambda$ CDM flat cosmology with  $\Omega_M = 0.3$ ,  $\Omega_\Lambda = 0.70$  and  $H_0 = 70 \text{ km s}^{-1} \text{ Mpc}^{-1}$ .

## 2 DATA

### 2.1 The S-PLUS galaxy catalogue

The S-PLUS (Southern Photometric Local Universe Survey)<sup>2</sup> aims to map  $\sim 9300 \text{ deg}^2$  of the Southern Sky using 12 optical bands (5 broad and 7 narrow), from the Javalambre filter system (Cenarro et al. 2019). S-PLUS is performed by T80-South, a 0.82m robotic telescope, equipped with a 9k x 9k CCD camera (covering  $1.4 \times 1.4$  square degrees per image), located at the Cerro Tololo Interamerican Observatory (CTIO), Chile. A full description of the survey and its first results can be seen in Mendes de Oliveira et al. (2019).

We use for this work the S-PLUS Data Release 1 (DR1)<sup>3</sup>, which corresponds to a  $336 \text{ deg}^2$  field delimited by  $-60.0^\circ < \alpha < 60.0^\circ$  and  $-1.5^\circ < \delta < 1.5^\circ$ . As this work focuses on extragalactic objects, we disregarded regions west of  $\alpha = -45^\circ$  due to its proximity to the Galactic plane. The mean seeing of the survey is 1.5 arcsec and it is complete up to  $r = 21.38 \text{ AB}$  ( $S/N > 3$  at a  $3''$  aperture). We opt to consider galaxies up to  $r = 21.0 \text{ AB}$ . Nakazono et al. (2021) did the star-galaxy separation by using a random forest algorithm trained over SDSS spectroscopically confirmed objects, which is used in this work.

For the sake of homogeneity of the cluster selection process, it is important to select galaxies based on their absolute magnitude. Thus, the higher the maximum redshift, for a given flux limit, the brighter the apparent magnitude cut at low redshift is. For that reason, we decided to limit this first catalogue to  $z = 0.4$ . At this redshift, the r-band flux limit corresponds to  $M = -20.5$ , which

<sup>1</sup> [https://github.com/stephanewerner/SPLUS\\_GalaxyClusterCatalogue](https://github.com/stephanewerner/SPLUS_GalaxyClusterCatalogue)

<sup>2</sup> [www.splus.iag.usp.br](http://www.splus.iag.usp.br)

<sup>3</sup> The S-PLUS DR1 can be assessed from: <https://datalab.noao.edu/splus/>

is about one magnitude fainter than the typical  $M_*$  characteristic magnitude (Puddu et al. 2021).

The photometric redshifts were produced using BPZ (Benítez 2000) as detailed in Molino et al. (2020). It was found that for  $z < 0.4$ , S-PLUS DR1 has a bias between the spectroscopic and photometric redshifts of 0.003, precision of  $\delta_z/(1+z) = 0.026$  and a 2.9% fraction of outliers. For the red galaxy population, which is about one-third of all galaxies up to that redshift and tends to dominate the cores of the clusters, those numbers are even more impressive: bias = -0.001,  $\delta_z/(1+z) = 0.018$  and outlier fraction = 0.5%. Those numbers confirm what we mentioned before that, given its 12 filter configuration, S-PLUS photometric redshift quality is one of its most appealing features.

## 2.2 The mock galaxy catalogue

To assess the performance of PzWav for S-PLUS type data and optimise its parameters, we created a mock catalogue from a simulated lightcone. The full description of the simulation can be found in Araya-Araya et al. (2021). Here we focus on the mock catalogue.

A wide lightcone with a projected area of  $324 \text{ deg}^2$  was created to simulate S-PLUS DR1 data. The synthetic galaxies were created using the Henriques et al. (2015) version of the L-GALAXIES semi-analytical model (SAM). This SAM uses as skeleton the Millennium Run (MR) simulation (Springel et al. 2005) scaled by the Planck I cosmology Planck Collaboration et al. (2014) using the Angulo & White (2010) algorithm. This algorithm generates a matter density field equivalent to that of running MR but in the Planck I cosmological framework.

We generate celestial coordinates using Kitzbichler & White (2007) techniques. Cosmological redshift estimation assumes that all galaxies at comoving distance  $d_C(z_i) < d_{C,gal} < d_C(z_i) + 30 \text{ kpc}$  are at redshift  $z_i$ . Finally, the ‘‘observed’’ redshift is computed by adding the peculiar motions of the galaxies to their cosmological redshifts. To do this, we estimate the radial velocities according to the galaxy velocity vectors (SAM output) and the line-of-sight.

Apparent magnitudes were estimated in the *post-processing* routine (Shamshiri et al. 2015). This technique consists of using the star formation histories arrays (SFHs) extracted from the SAM output, which stores information about the mass of new stars between two cosmic times and the metal mass of these new stars. Since for each cosmic time we have the quantity of the new stars and metals, we can assume that each SFH bin represents a given stellar population. Therefore, we can attribute on particular spectral energy distribution (SED) to each SFH bin.

The SED templates are those from the Maraston (2005) stellar synthesis population models, assuming an Chabrier (2003) initial mass function. The template set corresponds to  $4 \times 221$  SEDs, for 4 different metallicities and 221 ages. Then, the total galaxy SED is derived as the sum of all SED linked to all SFH bins. Dust extinction models are also applied over galaxy SEDs. For those, we have used the same extinction models as in Henriques et al. (2015), Shamshiri et al. (2015) and Clay et al. (2015). Since we have not included the luminosity contribution of emission lines into the galaxy SEDs, we cannot emulate narrow-band photometry properly. Therefore, we only compute apparent magnitudes in the five S-PLUS broad-band filters, which correspond to the u, g, r, i, and z filters of the Sloan (Fukugita et al. 1996) in the AB system.

In general, SAMs fail to model galaxies that reside in low mass halos due to the mass resolution of the base dark matter simulation ( $m_p = 9.6 \times 10^8 M_\odot/h$ , for MR (scaled Planck cosmology)). We expect small halos to be abundant, which implies that the SAM

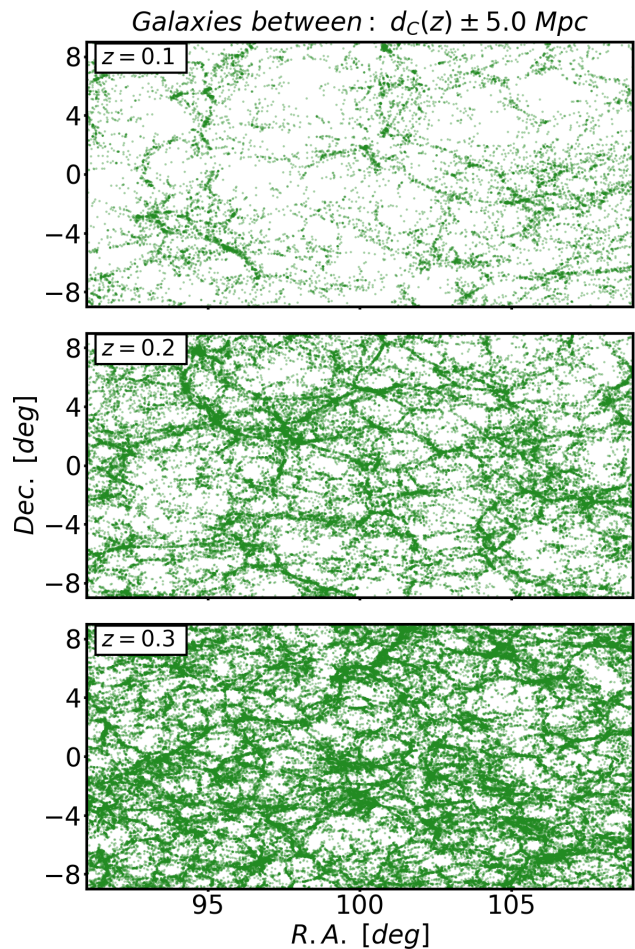


**Figure 1.** Spatial distribution of mock galaxies within redshift slices centred at  $z = 0.1, 0.2,$  and  $0.3$  (from top to bottom panel) and  $5 \text{ Mpc}$  width.

predicts many low mass objects with no reliable characteristics. For instance, Merson et al. (2013), who used another SAM, only included galaxies with stellar masses greater than  $M_* = 10^9 M_\odot/h$  in their mock. However, as shown in Henriques et al. (2015), the version of L-GALAXIES used here can reproduce observational results satisfactorily for galaxies with a stellar-mass higher than  $10^8 M_\odot/h$  at low redshift and this was the lower limit adopted here as for the mock galaxies.

### 2.2.1 Mock galaxy cluster sample

The catalogue of galaxies was extracted from the Virgo-Millennium<sup>4</sup> database. We selected all dominant dark matter halos (MPAHaloTrees.MRscPlanck1 table; haloId = firstHaloInFOFgroupId) with  $m_{\text{crit}200} \geq 10^{13.5} M_\odot$ . This quantity represents the mass within the radius where the halo presents an overdensity 200 times the critical density of the Universe. Each galaxy into the lightcone also has the identifier haloId, which links to the dark matter halos where it resides. Therefore, we obtain the spatial coordinates of the halos as the median of the hosted galaxy positions. Finally, we found within the  $324 \text{ deg}^2$  mock catalog, for  $z \leq 0.44$ :

<sup>4</sup> <http://gavo.mpa-garching.mpg.de/MyMillennium/>

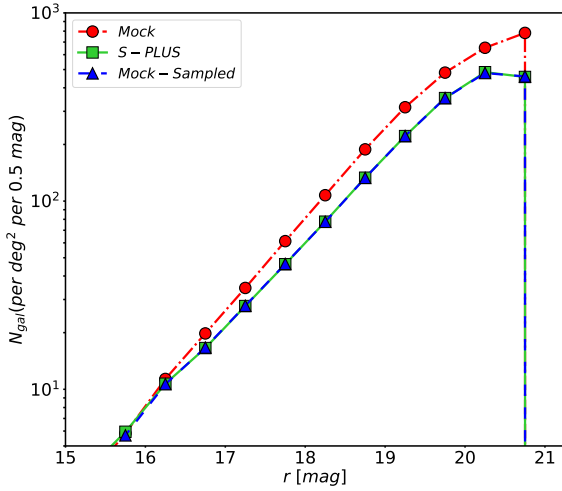


**Figure 2.** The  $r$ -band galaxy number counts of galaxies at  $z < 0.44$  the original (red points; dash-dotted line) mock compared to S-PLUS data (green squares; solid). The blue triangles; dashed line show the distribution for the mock after applying the sampling technique described in section 2.2.2.

5618 massive groups ( $13.5 < \log(M_{200}/M_{\odot}) < 14.0$ ), 1177 low-mass galaxy clusters ( $14.0 < \log(M_{200}/M_{\odot}) < 14.5$ ), and 151 intermediate/massive clusters ( $14.5 < \log(M_{200}/M_{\odot}) < 15.0$ ).

### 2.2.2 Galaxy number counts

In order to perform a reliable analysis, the observed and simulated catalogues have to be mutually consistent. However, by comparing the galaxy number counts in both, we found a 40% excess in the mock catalogue in relation to the S-PLUS (see Figure 2). We proceed in the following way to correct such a discrepancy.

First, we define a selection function,  $s(m)$ , which quantifies the galaxy excess per square degree in the lightcone compared to S-PLUS data at a given magnitude:

$$s(m) = \frac{n_{\text{mock}}(m) - n_{\text{S-PLUS}}(m)}{n_{\text{mock}}(m)}, \quad (1)$$

where  $n_{\text{mock}}(m)$  and  $n_{\text{S-PLUS}}(m)$  denote the number of galaxies with magnitude  $m$  per square degree in the mock and S-PLUS, respectively. In principle, we obtain  $n_{\text{mock}}$  and  $n_{\text{S-PLUS}}$  counting the number of galaxies within magnitude bins of width 0.25 mag normalized by the sky area. We compute the selection function by using the  $r$ -band as a base, whose limits are from 14 mag and 21 mag (in both mock and S-PLUS data).

The second step is to interpolate  $s(m)$  at the magnitude of each simulated galaxy,  $m_i$ , to reduce the effect induced by the binning. Later, we attribute each one a random value,  $p_i$ , following a uniform distribution. Finally, if  $p_i \leq s(m_i)$ , we exclude the galaxy from the sample. In Figure 2, we present the result of this routine, which is a mock with  $r$ -band galaxy number counts indistinguishable from the obtained with S-PLUS data.

Notice that this process randomly excludes galaxies depending only on their magnitudes, independent of spatial distribution or galaxy populations. In fact, the achieved accuracy of cluster detection could change for different sample realizations. For this reason, we will perform our analysis using ten sampled mocks.

### 2.2.3 Photometric redshift attribution

To properly match the S-PLUS data and the mock catalogue, we need to assign redshift probability density functions to mimic photo-zs. We cannot estimate them from the mock apparent magnitudes as the simulation is unable to produce values for the narrow bands. The procedure adopted was to use its magnitudes as a predictor of the smearing the photometric technique would cause on the mock true redshift values, considering that in different magnitude bins we have different redshift errors.

From the work of Molino et al. (2020) we got a relation between the  $r$ -band magnitude and the normalized median absolute deviation of the photo-zs compared to the spectroscopic redshift,  $NMAD(r)$ . The mock photo-z central value is a random number generated from a Gaussian distribution, centred on the true redshift and assuming  $NMAD(r)$  as its standard deviation. The  $P(z)$  will be the same Gaussian but centred on the drawn photo-z central value. Given the low incidence of photo-z outliers, we did not include this feature in the mock.

## 3 THE PZWAV ALGORITHM

The PzWav (Gonzalez 2014; Euclid Collaboration et al. 2019) is a code that uses the geometrical distribution of galaxies to find overdensities of galaxy luminosity in the sky. It was inspired by previous work for the Spitzer Infrared Array Camera (IRAC) Shallow Cluster Survey (Elston et al. 2006; Eisenhardt et al. 2008). The code requires a catalogue of sky coordinates, apparent magnitudes, and the redshift probability distribution functions  $P(z)$  for each galaxy. The algorithm works by creating smoothed density maps for redshift slices and searches for density peaks in each slice. The centre of each cluster is defined as a peak on these maps and its redshift is estimated using the probability distribution of the galaxies within a fixed radius.

First, with the code fed by the information of galaxies distributed in a certain redshift range, it creates a set of redshift slices and the galaxies on them. Each galaxy contributes to each slice according to the total probability of being in that slice, given by  $P(z)$ . An illustrative example is shown in Figure 3, where three contiguous redshift slices are shown for an area of  $1.4 \text{ deg}^2$  of the S-PLUS/DR1 among which individual galaxy contributions are spread.

The smoothing kernel approach used on these slices is such that it excludes very small structures such as galaxies and small groups, and the effects of the large-scale structure. To match clusters scales, we used 0.5 and 1.4 Mpc as the small and large scales, respectively. This approach is known as Difference-of-Gaussians (DoG), a kernel frequently used in image science for edge and blob detections. It is a practical implementation of the Laplacian of the Gaussian or the Mexican hat wavelet, and hence the name of the code.

Second, with a set of identified peaks in the slices, the PzWav evaluates those that lie near in spatial distribution (RA, Dec,  $z$ ) and consider the strongest one as representative of a given clustering. This is done to avoid double counts of merging systems. Additionally, we also reject peaks identified near the edge of the survey area to avoid border detection artifacts.

Finally, once the clusterings are identified, another set of density maps is created to calculate uniform noise thresholds as a function of the redshift. The final output has, for each peak: the sky coordinates, the redshift, a proxy for richness, peak rank, and the detection signal-to-noise ratio. The noise level is a Gaussian approximation based upon the distribution of the peak heights of

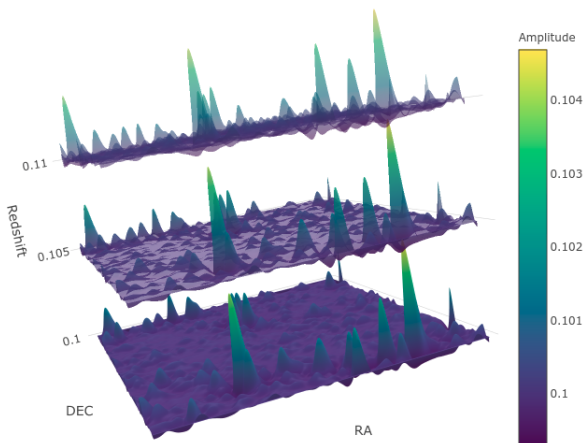


**Figure 3.** PzWav density of galaxies maps for three redshift slices.

Parameter	Description	Value
DZ	Width of the redshift slices	0.005
ZSTEP	Redshift spacing between slices	0.001
SCALE1	Small scale of the DoG kernel	500 kpc
SCALE2	Large scale of the DoG kernel	1400 kpc
DET_THRESH	Peak finder detection threshold	0.25
DRLIM	Max. projected separation to merge	1500 kpc
DZLIM	Max. redshift separation to merge	0.030

**Table 1.** PzWav main parameters and respective values adopted for this work.

fluctuations in the random maps, from which the standard deviation is calculated. The SNR is then simply defined as the ratio of the peak height for a given detection relative to the noise level in the random maps.

The version of PzWav used for S-PLUS differs somewhat from the version used by the Euclid collaboration, as this project uses a version of the code that branched prior to refinement and incorporation of PzWav for the Euclid mission. The code has a small number of parameters, which are designed to optimise its performance for the characteristics of each input data set. The main departure from the Euclid Collaboration et al. (2019) configuration is DZ and ZSTEP. Given the better photo-z accuracy of S-PLUS when compared with the expectation for broad-band photometric redshifts, the redshift slicing can be made substantially narrower. ZSTEP is the redshift space between slices. SCALE1 and SCALE2 are the minimum and maximum scales used to detect the structures. DET\_THRESH is the minimum size of the peak to detect it as a structure. DRLIM is the minimum projected separation to merge, if the separation between two structures is smaller than this value they are considered only one structure. DZLIM is the minimum redshift separation to merge, if the value is lower than that, we consider the two structures as only one. Table 1 summarizes the choices we made for this work.

#### 4 PZWAV PERFORMANCE ASSESSMENT OVER SIMULATED DATA

In this section, we apply PzWav over the S-PLUS like, mock catalogue. The aim here is to find the best set of parameters and assess the code performance, mainly the output catalogue completeness

and purity as a function of its minimum detection signal-to-noise ratio.

#### 4.1 Matching procedure

As a first step in the assessment procedure, we describe two techniques to match the PzWav detected peaks to clusters in the mock catalogue: the *geometrical matching* and the *ranking matching*, as described in Euclid Collaboration et al. (2019).

The *geometrical matching* starts with linking mock clusters and PzWav peaks by distance. We use a 1.5 Mpc search radius and a maximum redshift separation of  $\Delta z = 0.06$ . The latter represents the maximum uncertainty in the S-PLUS sample redshifts considering Molino et al. (2020). In the case of multiple matches, the closest one is the only one kept. This is done twice. Each time one of the catalogues is the reference, while we search for counterparts in the other. We consider successful matches the pairs formed in both directions.

The *ranking matching* assumes that more massive structures are the easy ones to be detected. While the geometrical technique is two-way, ranking matching is a one-way association. With the mock catalogue as the reference, we search for counterparts in the detection catalogue within the same volume definition as for the geometrical matching. However, a few mock clusters have a similar detected counterpart. To choose the final match we order the previous generated table in terms of detected richness and mass. Once we have the two tables, if two mock clusters have the same observed counterpart, we match the richest one with the most massive one.

These two methods resulted in mock-detection catalogues that largely agree with one another if we use a low-mass threshold ( $\log(M/M_\odot) > 13.0$ ). If we use high-mass thresholds, however, ranking matching returns greater completeness ( $\log(M/M_\odot) > 14.0$ ). From here on, we assume the ranking matching catalogue of detections for our analysis.

#### 4.2 Fragmentation and Overmerging

We define the N-fragmentation rate and the N-overmerging rate to evaluate how well the technique applied here recovers the clusters. The N-fragmentation rate is defined as the fraction of the mock clusters that have more than N counterparts with the detected cluster. The N-overmerging rate is the rate of detected clusters that have more than N counterparts with the mock clusters.

We used a cut for detections having  $S/N > 3.0$ . The fraction of objects with more than one counterpart (considering N-fragmentation and overmerging) is less than 1% in all mass ranges ( $13.5 < \log(M_{200}/M_\odot) < 15.0$ ). For 4 or more counterparts, this rate falls to  $\approx 0.01\%$ . In the high-mass end,  $\log(M_{200}/M_\odot) > 14.8$ , it is less than 0.001%. These values agree with previous estimates using the Euclid mock (Euclid Collaboration et al. 2019). This result means that our technique does not fragment structures or merge different structures of the mock.

#### 4.3 Centre and redshift

The estimated centres and redshifts of the clusters may be compared with the ones of the mock catalogue to evaluate the quality of the detections. We evaluate the cases of clusters having mass ( $M_{200}$ ) greater than  $10^{14} M_\odot$ . We did it by comparing the mean and standard deviation ( $1\sigma$ ) of the centres considering their RA and DEC and  $\frac{z_{PzWAV} - z_{true}}{1 + z_{true}}$ . The mean of the difference between centres is

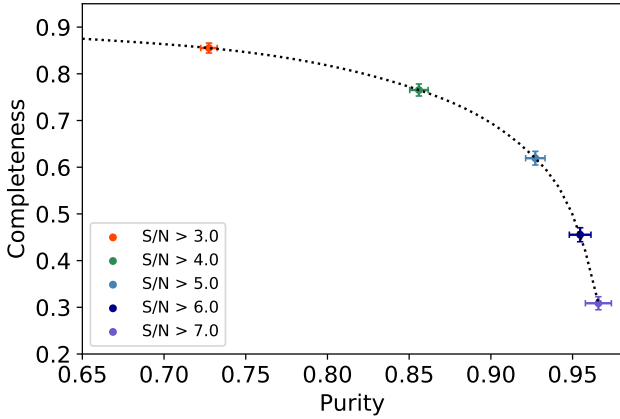


**Figure 4.** Completeness and purity as a function of the minimal signal-to-noise ratio for clusters with  $M_{200} > 10^{14}M_{\odot}$  and  $0.1 < z < 0.4$ . The dotted line connecting the points is used to guide the eyes. The values were estimated using the mean completeness and purity for the 10 mocks.

$0.010Mpc$ , with a standard deviation of  $0.012Mpc$ . For the redshifts, the mean of the difference is  $0.6 \times 10^{-3}$  and the standard deviation is  $8.8 \times 10^{-3}$ . By doing this, we find that there is a good agreement between the found clusters and the real clusters for most of the cases.

#### 4.4 Completeness and Purity

By comparing the PzWav detections over the mock with the, already known, catalogue of clusters present on it, we are able to determine both purity and completeness: purity is the number of true positive detections over the total detections number and completeness is the number of true positive detections over the total number of clusters in the simulation.

As quality statistics, purity and completeness are not independent and depend on the minimal signal-to-noise ratio ( $S/N_{min}$ ) used to select a cluster sample. Figure 4 shows their values for clusters with masses greater than  $M_{200} > 10^{14}M_{\odot}$  and redshifts in the range of  $0.1 < z < 0.4$ , to different cases of  $S/N_{min}$ .

As expected, the more stringent the  $S/N$  cut is, the purer and less complete the sample is – and *vice versa*. At  $S/N > 3.3$  the continuous, interpolated, purity-completeness curve is at its minimum Euclidean distance to the perfection (100% pure and complete). Here we adopt this as  $S/N > 3.3$  *bona fide*. Under this cut, the PzWav cluster catalogue is 82% complete and pure.

In Figure 5 we plot the variation of the completeness and purity for mock clusters with  $M_{200} > 10^{14}M_{\odot}$  and PzWav detection  $S/N > 3.3$ , for different redshift ranges. For the lowest redshift bin,  $z < 0.1$ , both statistics are poorer, with the completeness dropping to  $\sim 80\%$  and purity to  $\sim 76\%$ . From all the other redshift slices the values of the statistics approach the combined values, quoted before.

The performance is relatively poor for  $z < 0.1$ . This is due to the fact that the photometric redshift errors are of the order of the photometric redshift values. While the matter in question should be revisited, for the present work we will work around this problem considering only clusters with  $z > 0.1$  for our main analysis – as we did already in Figure 4. It is also important to mention that the completeness for  $0.35 < z < 0.40$  is lower due to the shallowness

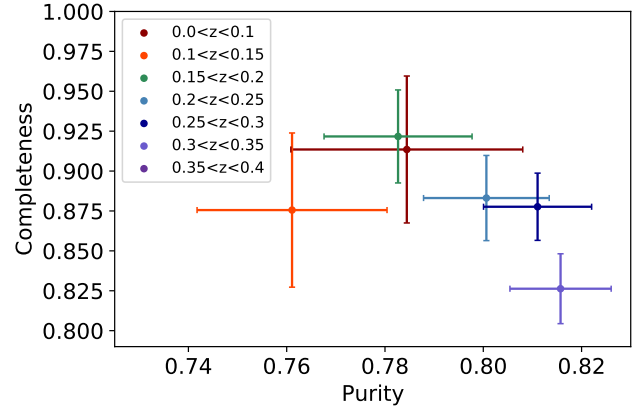


**Figure 5.** Completeness and purity in slices of redshift for mock clusters with  $M_{200} > 10^{14}M_{\odot}$  and PzWav detection  $S/N > 3.3$ . The values were estimated using the mean completeness and purity for the 10 mocks.

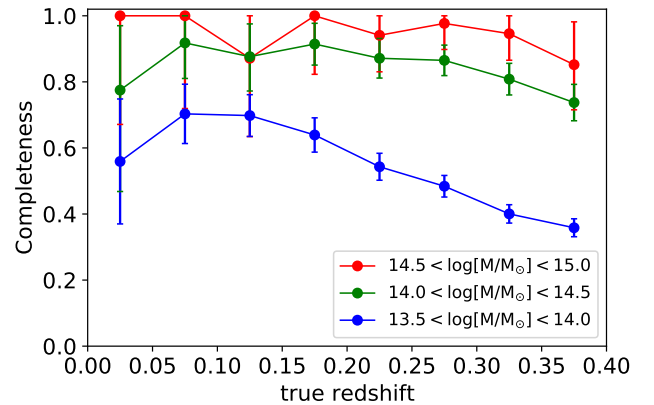


**Figure 6.** Completeness as a function of redshift in three mass ranges, with PzWav detection  $S/N > 3.3$ . The values were estimated using the mean completeness and purity for the 10 mocks.

of S-PLUS data and difficulty at detecting galaxies at the higher redshifts.

In this work, we do not estimate the masses for all detected clusters and due to that, we do not have a way to estimate the purity as a function of mass. We know the masses for the mock clusters, but we do not know the masses for all the detected clusters because we have a fraction of detected clusters that are not real. Due to that, we only do this analysis for the completeness. Figure 6 shows the completeness as a function of redshift in three mass ranges. In the cluster mass range  $M_{200} > 10^{14}M_{\odot}$ , completeness is above 80% in all cases, except for the highest redshift bin ( $0.30 < z < 0.40$ ) for low mass clusters ( $14.0 < \log(M_{200}/M_{\odot}) < 14.5$ ). Its value also tends to be constant up to  $z = 0.25$ , and then slowly falls. In the galaxy group mass range ( $13.5 < \log(M_{200}/M_{\odot}) < 14.0$ ), however, completeness is never higher than 70% and falls sharply with increasing redshift.

##### 4.4.1 Effects of the photometric redshifts

Simulations with the mock galaxy data allow us to test the consequences of changing the accuracy of the photometric redshift

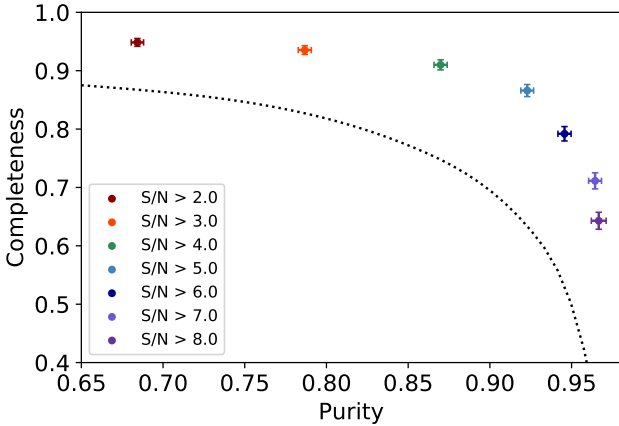


**Figure 7.** Completeness vs purity using the real redshifts of the simulation as a function of the minimal signal-to-noise ratio for clusters with  $M_{200} > 10^{14} M_{\odot}$  and  $0.1 < z < 0.4$ . The dotted line is what we found using our simulated photometric redshifts, the same curve as in Figure 4.

measurements. For example, the method may be tested for a perfect redshift estimate when the true redshifts of the simulation is used. By doing this, we reach more than 85% purity and completeness for a range of signal-to-noise thresholds, as presented in Figure 7. In the same context, we expect very accurate photo- $z$ 's from the Javalambre Physics of the Accelerating Universe Astrophysical Survey (J-PAS) due to its set of 56 filters (Bonoli et al. 2021). This improved redshift data would produce a galaxy cluster catalogue with purity and completeness between the ones obtained for  $z_{true}$  and usual  $z_{phot}$  as available from the already carried out surveys.

#### 4.5 S/N and halo mass correlation

We estimate the correlation between the  $S/N$  and  $M_{200}$  for clusters with  $S/N > 5.0$  using a non-linear least squares technique. Considering all redshift ranges we found that  $S/N = 0.37 * (\log(M_{200})) - 4.41$ . However, this correlation have a high dispersion and it is sensitive to the redshift range as can be seen in Figure 8.

## 5 THE CLUSTER CATALOGUE

We applied PzWav to the S-PLUS DR1 data. The result is a main catalogue with 4499 detections with  $S/N > 3.3$  in the range  $0.10 < z < 0.40$ . We considered only objects with  $-1.3^{\circ} < \delta < 1.3^{\circ}$  to remove border effects, and with  $-45^{\circ} < \alpha < 60^{\circ}$  to avoid the Galactic plane. In Figure 9 we show the projected spatial distribution. We also extent our analysis for a purer sample with  $S/N > 5.0$  doing membership analysis, comparison with a spectroscopic sample and search for new clusters. A sample of this catalogue is in Table 2 while the full version is available for download on a GitHub repository<sup>5</sup> and it will also be available soon on Vizier.

We are also making auxiliary catalogues available: the collection of low redshift ( $z < 0.1$ ) detections with  $S/N > 3.3$ , and a catalogue of objects in the full redshift range and detection with  $0.5 < S/N < 3.3$ . The eventual users of those catalogs must have

<sup>5</sup> [https://github.com/stephanewerner/SPLUS\\_GalaxyClusterCatalogue](https://github.com/stephanewerner/SPLUS_GalaxyClusterCatalogue)

in mind the limitations discussed in Section 4.4. The main and auxiliary catalogues are also available on GitHub.

Due to the fact that different surveys have different  $P(z)$  for the photometric redshifts, we had to adapt the PzWav code in order to optimize its performance when using S-PLUS data. As it was discussed in Molino et al. (2020), the presence of narrow unevenly spaced band filters in the photometric system creates artificial patterns in the redshift quality. In particular, when a galaxy has emission lines that fall in two of those filters, its redshift uncertainties are lower than most part of the sample, in other words, its  $P(z)$  will be much narrower than most galaxies with the same flux.

This sometimes extreme heteroscedasticity creates difficulties for PzWav. Objects with photo- $z$ 's much better than the average will have a large score ( $P(z)$  integrated over the limits of a given redshift slice) in a particular  $z$ -slice and it may result in clusters detection with a single, or very few, galaxies.

Before we work out a more general solution to this issue, we circumvented it. Instead of using the BPZ  $P(z)$ 's we generated Gaussian distributions, centred in the point-value estimate given by BPZ with a standard deviation  $\sigma = 0.028$ , which is the value for the galaxies that have magnitude  $r = 21$  AB (Molino et al. 2020)). Although we do not make full use of the information encoded in the full photometric redshift probability distribution function (pdf), a general solution is at this time beyond our objectives in this work. So we decided to make use of the Gaussian pdfs.

### 5.1 Comparison with other catalogues

We compared the catalogue generated with the PzWav with seven other catalogues that covered the same area – which is part of the well-investigated Stripe 82 (S82) area. All the comparison shown below are restricted to the  $0.1 < z < 0.4$  redshift range. We used a geometrical matching, as not all of them have parameters that allow for the use of ranking matches. The starting points are the previously detected objects. We opt for two configurations, a more strict one with a search radius of 1.0 Mpc and maximum redshift separation of  $\Delta z = 0.05$  and a broader one, with 1.5 Mpc and  $\Delta z = 0.1$ , respectively, to take into account uncertainties in the other catalogues, i.e., different catalogues have different errors in redshift and centre position.

In our sample, 128 groups and clusters have galaxies with spectroscopic redshifts in the literature. This information was used to measure how well PzWav estimates the cluster redshift. We found that the mean redshift residue is 0.0028 and the standard deviation is 0.0122. This is considerably low considering that the photometric redshift error for galaxies can be up to 0.03 (Molino et al. 2020).

Three of the catalogues of the S82 area, discussed here, are based on ICM observables. Two of them are based on X-ray emission: the XMM galaxy cluster survey (XCS; Mehrrens et al. 2012) and the XMM-Newton 3XMM/SDSS Stripe 82 Galaxy Cluster Survey (3XMM/SDSS; Takey et al. 2016, 2019). The third one is based on the S-Z effect data, and was derived from the ACTPol survey (Hilton et al. 2021). We also compared our catalogue with previous optical detections in the same area: RedMaPPer (Rykoff et al. 2014), WH15 (Wen & Han 2015) and GMB11 (Geach et al. 2011), based on SDSS data, and results of Durret et al. (2011), which uses the CFHTLS wide data. Table 3 shows the percentages of clusters in other surveys that we were able to recover from the S-PLUS data.

The X-ray/SZ catalogues can be considered effectively pure, as there are not many other possible contaminants in the sky for

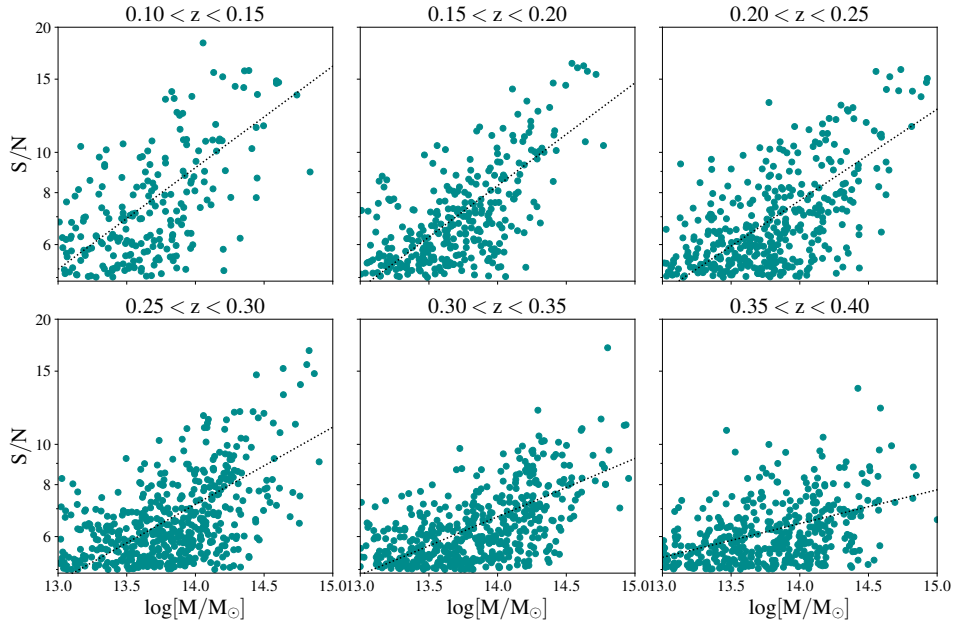


**Figure 8.**  $S/N$  vs  $\log[M/M_{\odot}]$  for mock clusters in different redshift ranges. The teal points represent the simulated clusters. The black dotted lines are the fitted functions.

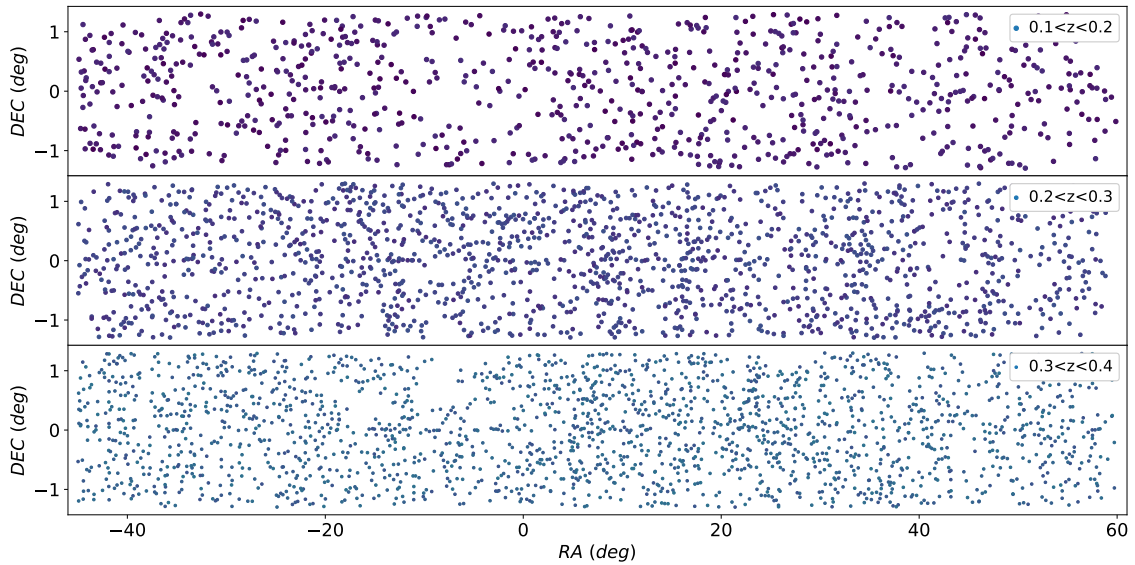


**Figure 9.** PzWav detected clusters with  $S/N > 3.3$  using S-PLUS data in the S82 area. In the upper panel there are clusters with  $0.1 < z < 0.2$ , in the middle panel  $0.2 < z < 0.3$  and lower panel  $0.3 < z < 0.4$ .

those, particularly in this relatively narrow redshift range and which is restricted to the local universe even excluding nearby galaxies (with  $z < 0.1$ ). Rykoff et al. (2014) also claim RedMaPPer/SDSS to be virtually complete and virtually pure ( $> 95\%$ ). Therefore, the number of matches considering these catalogues is a direct test of completeness in the mass range covered by the catalogues. Table 3 shows that PzWav/S-PLUS can indeed recover a high fraction of the objects in those samples: 56-89% and 61-97% for the strict and broad criteria, respectively.

Using the strict match of X-ray/SZ catalogues, we estimated the centre distances from our centre to these centres, the result is shown in Figure 10. The mean of the distribution is 240 kpc and the standard deviation is 170 kpc, considering the three catalogues. These values are considerably higher than the values found for the simulation (mean of 10 kpc and  $\sigma$  of 12 kpc). This can be explained by the fact that we estimate the centre as the distribution of the galaxies, while in these catalogues the centre is estimated considering the plasma distribution, and a difference of a few kiloparsecs is expected.



**Table 2.** Sample of the detected clusters. The full catalogue is available on GitHub and will be available on Vizier. The catalogue has further columns including  $M_{200}$ ,  $R_{200}$ , velocity dispersion, number of members, and if the cluster was found by previous catalogues. All the columns are shown in Table A1 in the appendix.

ID	RA (deg)	DEC (deg)	z	z error	S/N
SPLUS233740+001619	354.419	0.272	0.280	0.001	30.773
SPLUS002436+000137	6.150	0.027	0.370	0.001	30.285
SPLUS002303-000722	5.764	-0.123	0.153	0.003	30.098
SPLUS211852+003332	319.718	0.559	0.292	0.007	27.774
SPLUS234341+001846	355.923	0.313	0.266	0.004	27.268
SPLUS004617+000111	11.572	0.020	0.115	0.001	26.216
SPLUS015243+010003	28.180	1.001	0.236	0.004	25.446
SPLUS010445+000223	16.189	0.040	0.289	0.009	25.348
SPLUS215754+010516	329.478	1.088	0.331	0.006	25.110
SPLUS011510+001604	18.794	0.268	0.042	0.003	24.154
SPLUS213545+000910	323.941	0.153	0.135	0.005	23.647

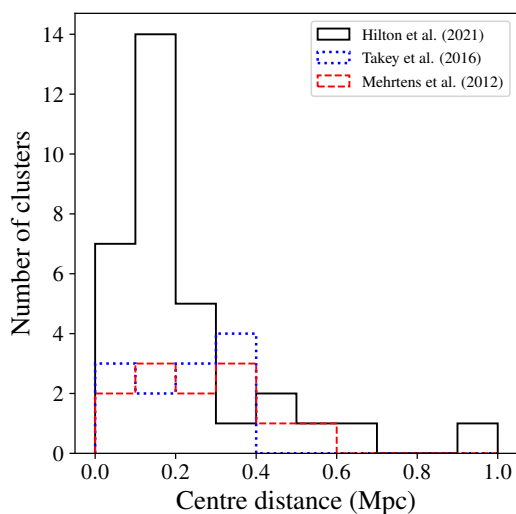


**Figure 10.** The cluster centre distance distribution using the X-rays and S-Z catalogues. In solid black, the matches with Hilton et al. (2021). In dotted blue, the matches with Takey et al. (2016) catalogue. In dashed red, Mehrstens et al. (2022).

The ACTPol survey focuses on the high mass end, with  $M_{500} > 4 \times 10^{14} M_{\odot}$ ;  $M_{200} \gtrsim 5.5 \times 10^{14} M_{\odot}$ . PzWav/S-PLUS is able to recover  $> 95\%$  ACTPol detections with the broad criteria and  $> 86\%$  criteria. This completeness is consistent with the results of the mocks, which predict more than 90% completeness for clusters with  $\log(M_{200}/M_{\odot}) > 14.5$  and more than 80% for clusters with  $\log(M_{200}/M_{\odot}) > 14.0$  (as shown in Figure 6).

The 3XMM catalogue is particularly useful as it has mass estimations ( $M_{500}$ ) for all its objects. By using  $M_{500} \sim 0.72M_{200}$  (Pierpaoli et al. 2003) one can see that the 3XMM sample is in the  $2.5 < M/(10^{13} M_{\odot}) < 34$  range, with an average of  $1.2 \times 10^{14} M_{\odot}$ . The PzWav/S-PLUS recovery rate (strict matching) is 23 out of 27 when considering only objects with  $M_{200} > 10^{14} M_{\odot}$ . This gives a completeness of 85%, which is roughly similar to the estimates from the mock analysis. Our recovery rate from the XCS sample is about as high as the others for the broad criteria (76%), but it is a lot smaller for the strict one (56%). Due to the fact that we do not have mass measurements for these clusters, we are not able to compare with results of Figure 6 in detail. We also attribute that to the uncertainty in the redshift as derived from photometric measurements.

The RedMaPPer/SDSS is limited, for purposes of building a

**Table 3.** Comparison between the current PzWav/S-PLUS catalogue of the Stripe 82 with other cluster catalogues of the same area, for objects with  $z \in [0.1, 0.4]$  in the first two columns and with  $z \in [0.1, 0.3]$  for the third and fourth columns. We used the geometrical match algorithm, starting from the previous catalogues and found possible matches in the PzWav/S-PLUS one. We adopted two criteria, a strict ( $R=1.0$  Mpc,  $\Delta z = 0.05$ ), and a broader one ( $R=1.5$  Mpc,  $\Delta z = 0.1$ ). The table shows that there is a redshift dependency on the detections, since the values for the last two columns are higher than the first two.

Catalogue	Match fraction (%)			
	Strict	Broad	Strict	Broad
ACTPol (SZ)	89	97	86	95
3XMM/SDSS (X-Ray)	74	85	81	88
XCS (X-Ray)	56	76	61	78
RedMaPPer/SDSS (Optical)	85	95	93	98
RedMaPPer/DES (Optical)	87	94	94	98
WaZP/DES (Optical)	40	60	50	64
WH15 (Optical)	62	75	72	77
GMB11 (Optical)	47	63	51	67
Durret11 (Optical)	30	63	33	64

References to the catalogues: ACTPol: Hilton et al. (2021); 3XMM/SDSS: Takey et al. (2016, 2019); XCS: Mehrstens et al. (2012), RedMaPPer/SDSS: Rykoff et al. (2014); RedMaPPer/DES: Rykoff et al. (2016); WaZP/DES: Aguena et al. (2021) WH15: Wen & Han (2015); GMB11: Geach et al. (2011); Durret11: Durret et al. (2011).

well defined sample, to a richness  $\lambda > 20$  or  $M \gtrsim 10^{14} M_{\odot}$  (Rykoff et al. 2014). The fraction of those clusters recovered by PzWav/S-PLUS is strikingly similar to the ones recovered from 3XMM: 85% and 95% (strict and broad criteria, respectively). In Figure 11 we show matches between both catalogues, in both directions. For the sake of reference, the SDDS coadded images of the Stripe 82 are about 1-2 magnitudes deeper than S-PLUS, depending of the band (Mendes de Oliveira et al. 2019).

A comparison with the RedMaPPer/SDSS catalogue is shown in Figure 11. About 4.1% of the RedMaPPer/SDSS clusters in the redshift range  $0.1 < z < 0.3$  are not in the catalogue. This number increases to 28.8% for  $0.3 < z < 0.4$ . On the other hand, the PzWav/S-PLUS cluster catalogue has many more objects. For the lower redshifts, it can be seen that RedMaPPer would only detect objects with high S/N. It means that our current catalogue reaches well within the galaxy groups mass range, below  $10^{14} M_{\odot}$ .

There are other optical catalogues of this same area, such as WH15 (Wen & Han 2015), GMB11 (Geach et al. 2011), and Durret11 (Durret et al. 2011). As they also have their own different completeness and purity levels within our range of interest, the comparison between our catalogue and those are not as straightfor-

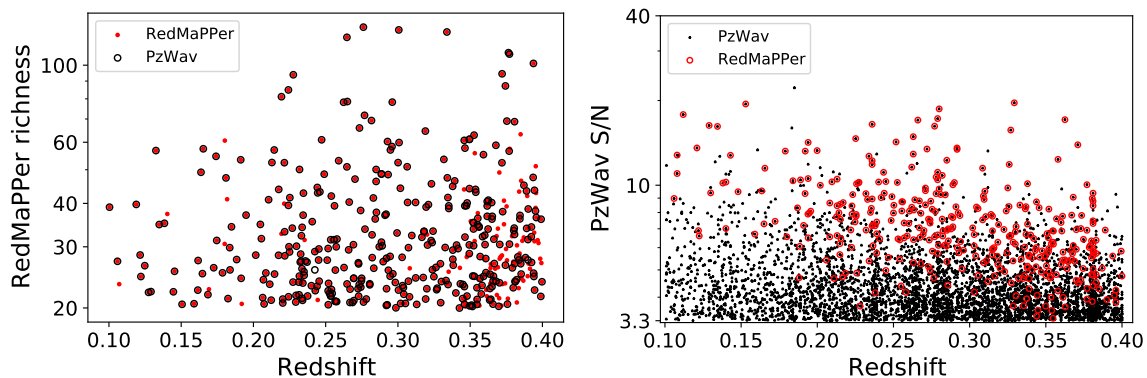


**Figure 11.** *Left Panel* - RedMaPPer/SDSS clusters in the redshift–richness space (red squares). The red rings correspond to PzWav/S-PLUS matches. *Right Panel* - PzWav/S-PLUS clusters in the redshift–signal to noise space (black squares). The black rings correspond to RedMaPPer/SDSS matches. The right panel demonstrates that the PzWav approach on our SPLUS DR1 data is able to successfully uncover beyond our S/N cut many clusters at lower S/N levels, when compared to RedMapper/SDSS clusters.

ward. We also include in Table 3 the fraction of the objects in those catalogues, that we also have in the PzWav/S-PLUS one.

Figure 11 also highlights that the selection based on signal-to-noise presented here is conceptually different than a member based on, such as in SDSS. While the former will produce a catalogue with the maximum number of objects, including several objects in the group mass range, in low redshifts, the latter allows for samples with more defined mass thresholds.

The match fractions are higher for clusters with  $0.1 < z < 0.3$  than for  $0.1 < z < 0.4$ , when considering  $S/N > 3.3$ . This shows that there is a redshift dependency on the detections and we do not find objects at  $0.3 < z < 0.4$  due to the shallowness of the data at this redshift range.

We compared the  $S/N$  of the detected clusters with the richness provided by each literature catalogue. We found a correlation for all catalogues as can be seen in the black lines of Figure 12. The correlation is spread as expected using the simulations as shown in Figure 8.

## 5.2 Photometric Membership

We apply a machine learning method to estimate a cluster membership probability, from which we obtain a membership classification. Our approach considers only photometric information of galaxies lying along the line of sight of each cluster candidate. That was previously shown to be efficient for low ( $z \leq 0.1$ , Lopes & Ribeiro 2020) and high redshift clusters ( $z > 1$ , Jiménez-Teja et al. 2021).

### 5.2.1 True Cluster Membership

Before employing the machine learning method we need to build a galaxy sample of true members and interlopers along the line of sight of a subset of clusters. This data set can be used for training and validation purposes.

We used a sample of galaxies with spectroscopic redshifts compiled by Molino et al. (2020) to assess the photometric redshift precision of the S-PLUS survey, using the S82 region. This sample is a combination of many different surveys in that region, such as the SDSS, 2SLAQ, 2dF, 6dF, among others. In total we have 84003 galaxies with S-PLUS iDR3 photometric information and spectra available within the S82.

The first step before selecting member galaxies from the spectroscopic data is to obtain spectroscopic redshifts for the PzWav clusters. That is necessary to have a uniform determination of the cluster’s redshifts. Their redshift is derived with the gap technique described in Katgert et al. (1996). However, we employ a density gap (Adami et al. 1998; Lopes 2007; Lopes et al. 2009) that scales with the number of galaxies available. We apply this method to all galaxies within  $0.50 h^{-1}$  Mpc of the cluster centre. The cluster redshift is then given by the biweight estimate (Beers et al. 1990) of the galaxy redshifts of the chosen group. Then we proceed as described below.

We only considered clusters with spectroscopic redshifts ( $z_{spec-cl}$ ) smaller or equal to 0.2. We do so as the spectroscopic sample is approximately complete to  $r = 19.0$ , which is equivalent to  $m_r^* + 1$  at  $z = 0.2$ . As previously discussed in Lopes et al. (2009) we should sample at least down to  $m_r^* + 1$  in order to avoid biases in the membership selection and estimation of cluster parameters (such as velocity dispersion and mass).

We applied the “shifting gapper” procedure (Fadda et al. 1996) to select members and exclude interlopers. It is important to stress this method makes no hypotheses about the dynamical status of the cluster. We proceed as follows. For each cluster, we start by selecting all galaxies within  $2.50 h^{-1}$  Mpc (3.57 Mpc for  $h = 0.7$ ) and showing a velocity offset of  $|\Delta v| \leq 4000 \text{ km s}^{-1}$ . The “shifting gapper” procedure is based on the application of the gap-technique in radial bins, starting in the cluster center. The bin size is  $0.42 h^{-1}$  Mpc (0.60 Mpc for  $h = 0.7$ ) or larger to force the selection of at least 15 galaxies. Those not associated with the main body of the cluster are eliminated. This procedure is repeated until the number of cluster members is stable.

Once we have a member list we obtain estimates of velocity dispersion ( $\sigma_P$ ), as well as of the physical radius and mass ( $R_{500}$ ,  $R_{200}$ ,  $M_{500}$  and  $M_{200}$ ). Our “shifting gapper” approach is similar, but not identical to Fadda et al. (1996). The most important difference is the adoption of a variable gap, instead of a fixed one. The variable gap scales with the number of galaxies in the cluster region and the velocity difference of those belonging to the cluster. Further details can be found in Lopes et al. (2009, 2014).

It is also important to keep in mind that for the current paper we want to have a spectroscopic membership classification of all galaxies projected along the line of sight (not only those with

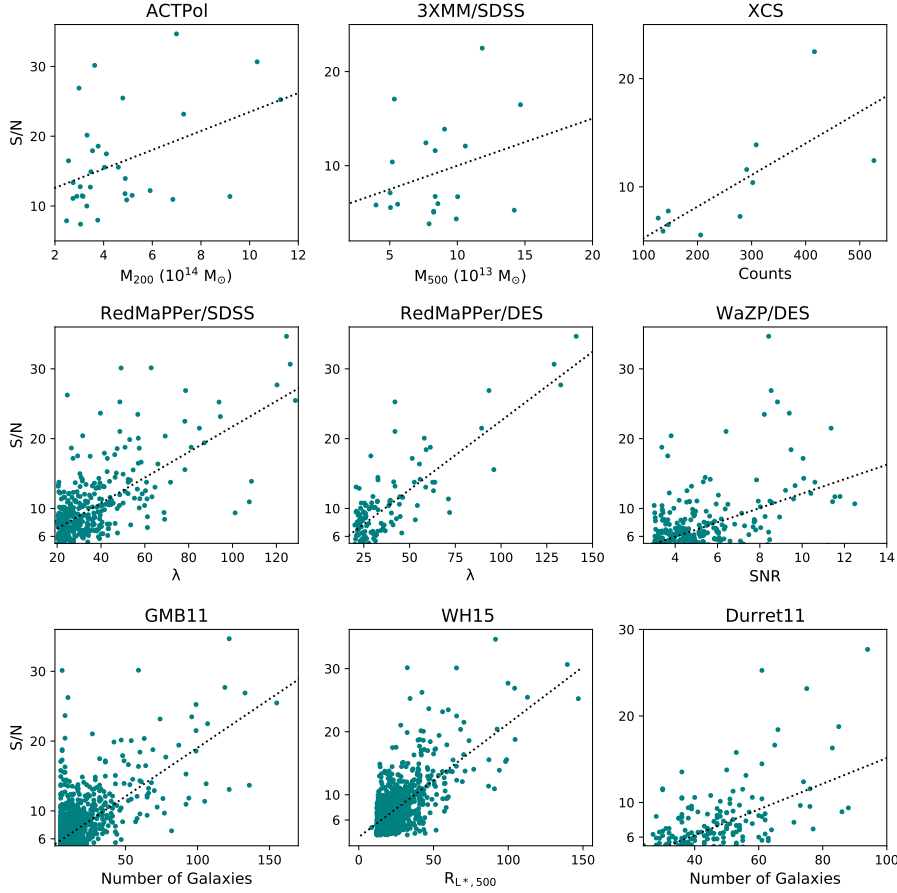


**Figure 12.**  $S/N$  vs mass or richness for literature catalogues. The teal dots are the matched clusters. The black dotted lines are the fits for each catalogue.

$|\Delta_v| \leq 4000 \text{ km s}^{-1}$ ). Hence, objects with  $|\Delta_v| > 4000 \text{ km s}^{-1}$  are automatically classified as interlopers (not members).

The final sample we have for training and evaluation purposes, within the 101 clusters, comprises 1838 galaxies (with  $r \leq 19.0$  and within  $R_{200}$ ).

### 5.2.2 Photometric Membership Through Machine Learning

We tested the performance of eighteen machine learning algorithms in Lopes & Ribeiro (2020), when we found six algorithms had superior performance. As in Jiménez-Teja et al. (2021) we found, for the current data set, the *Stochastic Gradient Boosting* (GBM) method shows slightly better results. That is assessed through the estimates of Purity (also known as "Precision" or "Positive Predictive Value", PPV) and Completeness (known as the "True Positive Rate", TPR or "Sensitivity"). Purity gives the fraction of true members among the objects classified as members, while Completeness is the fraction of true members that are classified as members.

Gradient boosting is a technique that can be used for regression and classification problems. The final model is an ensemble of weak prediction models, normally decision trees. However, differently than models based on *bagging*, methods in the form of *boosting* result in decreased classification bias, instead of variance. The *Stochastic Gradient Boosting* is the result of a modification proposed by Friedman (2002). He proposed that "at each iteration a subsample of the training data is drawn at random (without replacement) from the full training data set. This randomly selected

subsample is then used in place of the full sample to fit the base learner and compute the model update for the current iteration." This randomization process improves accuracy and execution speed, as well as increases robustness against the overcapacity of the base learner.

We expect galaxy members and interlopers projected along the line of sight of clusters to show different distributions of many parameters, such as colors and magnitudes, but also structural and environmental properties. That is shown in Figure 4 of Lopes & Ribeiro (2020). In the ML terminology, those parameters are called "features". As in Lopes & Ribeiro (2020) we ranked the features by 'importance', but also tested the performance of our algorithms with different choices of variables. We finally chose the following parameters for training and evaluating our results: (u-r), (g-i), (r-i), (r-z), (J0395-g), (J0395-r), (J0515-r), (J0430-i), (J0660-i), r, LOG  $\Sigma_5$ ,  $R/R_{200}$ ,  $\Delta_{z_{phot}}$ . The  $\Delta$  stands for an offset relative to the mean cluster redshift. As one of our features is the normalized cluster-centric distance ( $R/R_{200}$ ) we derive an estimate of  $R_{200}$ , using a scaling relation between this parameter and richness obtained within a fixed metric (0.50 Mpc).

Based on the parameters above we obtained high values of Completeness (C) and Purity (P),  $C = 92.1\% \pm 1.9\%$  and  $P = 85.7\% \pm 2.3\%$ . This method was then applied to all galaxies in the regions of the 628 cluster candidates with  $z_{phot} \leq 0.23$  (considering the photo-z errors, that is consistent to the spectroscopic redshift limit above;  $z = 0.2$ ). In total, we have 8467 galaxies with  $r \leq 19.0$  and within  $R_{200}$  of those 628 systems.

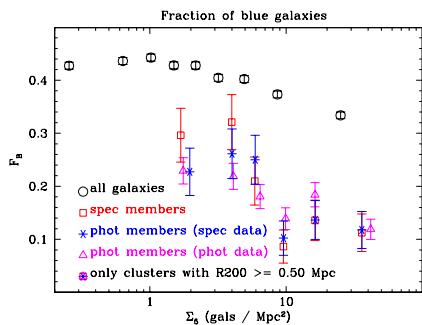


**Figure 13.** The fraction of blue galaxies as a function of the local galaxy density ( $\Sigma_5$ ). The black circles show the results for all galaxies lying along the line of sight of the 628 cluster candidates in our sample, including back and foreground objects. The red squares, magenta triangles, and blue asterisks show the fractions only for members and within  $R_{200}$ . The squares display results derived from the spectroscopic membership classification (using the 101 clusters with spectroscopic data), while the results for the asterisks are based on the same data set, but consider the photometric classification. The triangles display the results for photometric classified galaxies of the 628 cluster candidates. These three last results only consider the richest clusters (we actually make a cut in the value of  $R_{200}$ , being larger or equal to 0.50 Mpc, as  $R_{200}$  scales with richness.)

As an example of an application of our photometric membership classification, we show in Fig. 13 the fraction of blue galaxies for members spectroscopically classified (red squares) and photometric (blue asterisks, also for the spectroscopic data set). The magenta triangles show the results for the photometric members within the 628 cluster candidates, while the black circles display the results for all galaxies lying along the line of sight of those 628 cluster candidates in our sample.

We have also estimated how many objects (clusters and groups) of this sample do not have any members inside  $R_{200}$ . These systems correspond to 10.59% of the original sample and were considered false positives. 21.35% of the clusters have at least 10 members inside  $R_{200}$  and 43.58% have at least 5 members.

### 5.3 New Clusters

We measured the fraction of new clusters comparing our sample with objects in NED and SIMBAD databases and with the catalogues mentioned in Table 3. We selected all objects classified as cluster, group or brightest cluster galaxy and matched them if they were inside 4 arcminutes of our cluster centre. We did not use redshifts because some of these objects did not have redshifts in the database, so this is a conservative match. Comparing with other catalogues, we matched the clusters if they were inside 1Mpc and  $|z_{cat} - z_{cls}| / (1 + z_{cls}) < 0.05$ . In total, we have 1186 clusters with  $S/N > 5.0$ , and 134 of them are not in the literature (11.3%). About 1.4% of systems containing at least ten galaxies in our final sample are - to the best of our knowledge - new groups/clusters, with the fraction increasing to 2.4% when the threshold is set to five galaxies. This means that 9.5% of these objects are small groups or are not real objects. Most of the newly detected objects have  $S/N < 10$  and at higher redshifts, as can be seen in Figure 14. Figure 15 shows SPLUS015840-011627 and SPLUS003715+002246, two clusters detected by PzWav using S-PLUS data that are not in any other literature catalogue used in this work, neither in Simbad and Ned databases.

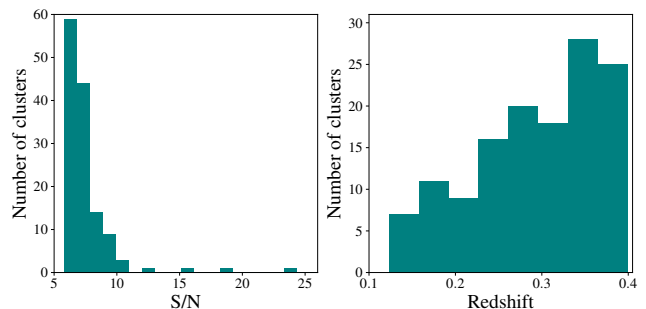


**Figure 14.**  $S/N$  and redshift distribution of new clusters. We used the catalogues of Table 3 and clusters of Simbad and NED databases to compare. Most new clusters have lower  $S/N$  and are at higher redshifts.

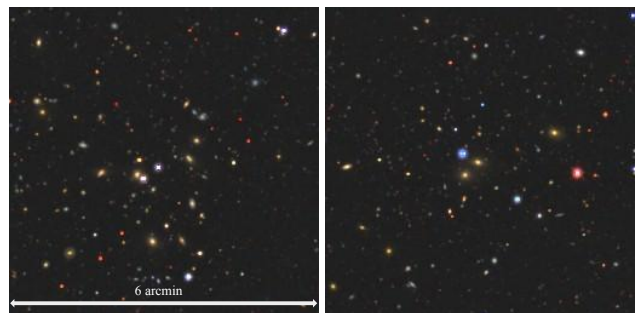


**Figure 15.** Images of clusters SPLUS015840-011627 (left) and SPLUS003715+002246 (right). These two clusters are not in the literature catalogues used in this work, nor in Ned and Simbad databases. SPLUS015840-011627 was detected at  $z \sim 0.18$  and SPLUS003715+002246 at  $z \sim 0.22$ . These images were obtained with the Legacy Survey.

## 6 CONCLUSION AND SUMMARY

The main goal of this work was to create a galaxy cluster and group catalogue using the S-PLUS DR1, with a tool that can be used to find clusters in the whole S-PLUS main survey. The tool used was the code PzWav, refined to work on S-PLUS data. We also applied PzWav to simulated lightcones in order to test and define the best parameters to be used in the search using the real data and to measure the purity and completeness of the catalogue. We used these parameters to find galaxy clusters and groups using S-PLUS DR1 data and produced a catalogue with 4499 objects for the Stripe 82 area.

The main findings of this work are:

- Based on the combined work on S-PLUS observations and our mock data, the resulting cluster and group catalogue reaches  $\sim 90\%$  of completeness and  $\sim 80\%$  purity, for suitable values of  $S/N$  and redshift interval, e.g. if  $S/N > 3.3$  and  $0.20 < z < 0.25$ , and if  $\log(M_{200}/M_{\odot}) > 14.0$ . A  $S/N$  cut of 3.3 within the range of  $0.1 < z < 0.4$  reaches more than 75% of purity and more than 80% of completeness.
- The percentage of clusters and groups that suffered of fragmentation and overmerging is less than 1% for at least 2 counterparts. It goes to  $\sim 0.01\%$  if we consider 4 counterparts.
- Comparing with X-ray/SZ catalogues, the standard deviation of the difference between the detected centres and the X-ray/SZ

centres is  $240 \pm 170$  kpc. For the simulations, we found that the standard deviation is 12 kpc for  $\log(M_{200}/M_{\odot}) > 14.0$ .

- Considering the clusters we have spectroscopic data,  $(z_{PZWAV} - z_{true})/(1 + z_{true})$  is less than 0.012. Using the simulations, this value is  $8.8 \times 10^{-3}$  for  $\log(M_{200}/M_{\odot}) > 14.0$ .

- The ACTPol catalogue is composed by very massive clusters detected with the S-Z effect, so we should find a high fraction of them. We found 86 – 97% of the ACTPol clusters, in agreement with the completeness expected by the simulations.

- Comparing with X-rays data, we found that using the 3MM/SDSS catalogue, we recovered 74% with a strict matching and 85% with a broad matching. Using the XCS catalogue, we recovered 56% for a strict matching and 76% for a broad matching.

- Comparing the PzWav output with the literature catalogues using optical data, we recover  $\sim 30$ –98% of each of them depending on the catalogue and matching criteria. Many clusters and groups that were not detected were in higher redshifts.

- We detected 1185 groups and clusters with  $S/N > 5.0$ , and 134 of them were not detected by the literature catalogues used in this work to compare and are not associated with galaxy clusters or groups in NED and Simbad databases.

We have a homogeneous sample to study galaxy properties and galaxy evolution, taking advantage of S-PLUS set of filters that were important to estimate photometric redshifts, and to give useful information about the science of galaxies. In the future, we plan to use the PDFs generated by machine learning photo-z codes to find clusters and groups in the next data releases. Moreover, we plan to apply the technique for a larger area of the sky, including areas that were not observed by any other survey yet ( $\sim 1000 \text{ deg}^2$ ). In the DR3, S-PLUS will map  $\sim 2000 \text{ deg}^2$ , and the future galaxy cluster and group catalogue will be useful for cosmological studies. We will also work on creating masks around bright objects to increase the purity of the sample.

## ACKNOWLEDGEMENTS

We thank the referee that gave useful comments to improve this paper. ESC acknowledges the support of the funding agencies CNPq (309850/2021-5) and FAPESP (2019/19687-2). The S-PLUS project, including the T80-South robotic telescope and the S-PLUS scientific survey, was founded as a partnership between the Fundação de Amparo à Pesquisa do Estado de São Paulo (FAPESP), the Observatório Nacional (ON), the Federal University of Sergipe (UFS), and the Federal University of Santa Catarina (UFSC), with important financial and practical contributions from other collaborating institutes in Brazil, Chile (Universidad de La Serena), and Spain (Centro de Estudios de Física del Cosmos de Aragón, CE-FCA). We further acknowledge financial support from the São Paulo Research Foundation (FAPESP), the Brazilian National Research Council (CNPq), the Coordination for the Improvement of Higher Education Personnel (CAPES), the Carlos Chagas Filho Rio de Janeiro State Research Foundation (FAPERJ), and the Brazilian Innovation Agency (FINEP).

The members of the S-PLUS collaboration are grateful for the contributions from CTIO staff in helping in the construction, commissioning and maintenance of the T80-South telescope and camera. We are also indebted to Rene Laporte, INPE, and Keith Taylor for their important contributions to the project. From CEFC, we thank Antonio Marín-Franch for his invaluable contributions in the early phases of the project, David Cristóbal-Hornillos and his team for their help with the installation of the data reduction package `JYPE`

version 0.9.9, César Íñiguez for providing 2D measurements of the filter transmissions, and all other staff members for their support with various aspects of the project.

This work was supported by Alpha Crucis, Yaci and UV30 that were used to run our codes. SW acknowledges Ivan Almeida for his helpful comments about the codes. ESC acknowledges financial support from the Brazilian agencies CNPq (PQ-308539/2018-4) and FAPESP (#2019/19687-2). PA-A thanks CAPES for supporting his PhD scholarship (project 88887.596140/2020-00). RLO acknowledges financial support from the Brazilian institutions CNPq (PQ-312705/2020-4) and FAPESP (#2020/00457-4). KMD thanks the support of the Serrapilheira Institute (grant Serra-1709-17357) as well as that of the Brazilian National Research Council (CNPq grant 312702/2017-5) and of the Rio de Janeiro State Research Foundation (FAPERJ grant E-26/203.184/2017), Brazil.

The Legacy Surveys consist of three individual and complementary projects: the Dark Energy Camera Legacy Survey (DECaLS; Proposal ID #2014B-0404; PIs: David Schlegel and Arjun Dey), the Beijing-Arizona Sky Survey (BASS; NOAO Prop. ID #2015A-0801; PIs: Zhou Xu and Xiaohui Fan), and the Mayall z-band Legacy Survey (MzLS; Prop. ID #2016A-0453; PI: Arjun Dey). DECaLS, BASS and MzLS together include data obtained, respectively, at the Blanco telescope, Cerro Tololo Inter-American Observatory, NSF’s NOIRLab; the Bok telescope, Steward Observatory, University of Arizona; and the Mayall telescope, Kitt Peak National Observatory, NOIRLab. Pipeline processing and analyses of the data were supported by NOIRLab and the Lawrence Berkeley National Laboratory (LBNL). The Legacy Surveys project is honored to be permitted to conduct astronomical research on Iolkam Du’ag (Kitt Peak), a mountain with particular significance to the Tohono O’odham Nation.

NOIRLab is operated by the Association of Universities for Research in Astronomy (AURA) under a cooperative agreement with the National Science Foundation. LBNL is managed by the Regents of the University of California under contract to the U.S. Department of Energy.

This project used data obtained with the Dark Energy Camera (DECam), which was constructed by the Dark Energy Survey (DES) collaboration. Funding for the DES Projects has been provided by the U.S. Department of Energy, the U.S. National Science Foundation, the Ministry of Science and Education of Spain, the Science and Technology Facilities Council of the United Kingdom, the Higher Education Funding Council for England, the National Center for Supercomputing Applications at the University of Illinois at Urbana-Champaign, the Kavli Institute of Cosmological Physics at the University of Chicago, Center for Cosmology and Astro-Particle Physics at the Ohio State University, the Mitchell Institute for Fundamental Physics and Astronomy at Texas A&M University, Financiadora de Estudos e Projetos, Fundação Carlos Chagas Filho de Amparo, Financiadora de Estudos e Projetos, Fundação Carlos Chagas Filho de Amparo a Pesquisa do Estado do Rio de Janeiro, Conselho Nacional de Desenvolvimento Científico e Tecnológico and the Ministerio da Ciencia, Tecnologia e Inovacao, the Deutsche Forschungsgemeinschaft and the Collaborating Institutions in the Dark Energy Survey. The Collaborating Institutions are Argonne National Laboratory, the University of California at Santa Cruz, the University of Cambridge, Centro de Investigaciones Energéticas, Medioambientales y Tecnológicas-Madrid, the University of Chicago, University College London, the DES-Brazil Consortium, the University of Edinburgh, the Eidgenössische Technische Hochschule (ETH) Zurich, Fermi National Accelerator Laboratory, the University of Illinois at Urbana-Champaign, the Institut de Cien-

cies de l'Espai (IEEC/CSIC), the Institut de Física d'Altes Energies, Lawrence Berkeley National Laboratory, the Ludwig Maximilians Universität München and the associated Excellence Cluster Universe, the University of Michigan, NSF's NOIRLab, the University of Nottingham, the Ohio State University, the University of Pennsylvania, the University of Portsmouth, SLAC National Accelerator Laboratory, Stanford University, the University of Sussex, and Texas A&M University.

BASS is a key project of the Telescope Access Program (TAP), which has been funded by the National Astronomical Observatories of China, the Chinese Academy of Sciences (the Strategic Priority Research Program “The Emergence of Cosmological Structures” Grant # XDB09000000), and the Special Fund for Astronomy from the Ministry of Finance. The BASS is also supported by the External Cooperation Program of Chinese Academy of Sciences (Grant # 114A11KYSB20160057), and Chinese National Natural Science Foundation (Grant # 12120101003, # 11433005).

The Legacy Survey team makes use of data products from the Near-Earth Object Wide-field Infrared Survey Explorer (NEOWISE), which is a project of the Jet Propulsion Laboratory/California Institute of Technology. NEOWISE is funded by the National Aeronautics and Space Administration.

The Legacy Surveys imaging of the DESI footprint is supported by the Director, Office of Science, Office of High Energy Physics of the U.S. Department of Energy under Contract No. DE-AC02-05CH1123, by the National Energy Research Scientific Computing Center, a DOE Office of Science User Facility under the same contract; and by the U.S. National Science Foundation, Division of Astronomical Sciences under Contract No. AST-0950945 to NOAO.

## DATA AVAILABILITY

The data underlying this article are available on GitHub at [github.com/stephanewerner/SPLUS\\_GalaxyClusterCatalogue](https://github.com/stephanewerner/SPLUS_GalaxyClusterCatalogue). It will be available soon on Vizier, Simbad and NED databases.

## REFERENCES

- Adami C., Mazure A., Biviano A., Katgert P., Rhee G., 1998, *A&A*, **331**, 493
- Agüena M., et al., 2021, *Monthly Notices of the Royal Astronomical Society*, **502**, 4435
- Allen S. W., Evrard A. E., Mantz A. B., 2011, *ARA&A*, **49**, 409
- Angulo R. E., White S. D. M., 2010, *MNRAS*, **405**, 143
- Araya-Araya P., Vicentin M. C., Sodré Laerte J., Overzier R. A., Cuevas H., 2021, *MNRAS*, **504**, 5054
- Ascaso B., Wittman D., Benítez N., 2011, *Monthly Notices of the Royal Astronomical Society*, **420**, 1167
- Balogh M. L., Morris S. L., Yee H. K. C., Carlberg R. G., Ellingson E., 1999, *ApJ*, **527**, 54
- Beers T. C., Flynn K., Gebhardt K., 1990, *AJ*, **100**, 32
- Bellagamba F., Roncarelli M., Maturi M., Moscardini L., 2017, *Monthly Notices of the Royal Astronomical Society*, **473**, 5221
- Benítez N., 2000, *ApJ*, **536**, 571
- Böhringer H., Werner N., 2010, *A&ARv*, **18**, 127
- Bonoli S., et al., 2021, *A&A*, **653**, A31
- Bykov A. M., Churazov E. M., Ferrari C., Forman W. R., Kaastra J. S., Klein U., Markevitch M., de Plaa J., 2015, *Space Sci. Rev.*, **188**, 141
- Cenarro A. J., et al., 2019, *A&A*, **622**, A176
- Chabrier G., 2003, *PASP*, **115**, 763
- Cibirka N., et al., 2017, *MNRAS*, **468**, 1092
- Clay S. J., Thomas P. A., Wilkins S. M., Henriques B. M. B., 2015, *MNRAS*, **451**, 2692
- Couch J. J., Ellis R. S., Malin D. F., MacLaren I., 1991, *MNRAS*, **249**, 606
- Cypriano E. S., Mendes de Oliveira C. L., Sodré Laerte J., 2006, *AJ*, **132**, 514
- Dalton G. B., Maddox S. J., Sutherland W. J., Efstathiou G., 1997, *MNRAS*, **289**, 263
- Dressler A., 1984, *ARA&A*, **22**, 185
- Durret F., et al., 2011, *A&A*, **535**, A65
- Eisenhardt P. R. M., et al., 2008, *ApJ*, **684**, 905
- Elston R. J., et al., 2006, *ApJ*, **639**, 816
- Euclid Collaboration et al., 2019, *A&A*, **627**, A23
- Fadda D., Girardi M., Giuricin G., Mardirossian F., Mezzetti M., 1996, *ApJ*, **473**, 670
- Friedman J. H., 2002, *Computational Statistics & Data Analysis*, **38**, 367
- Fukugita M., Ichikawa T., Gunn J. E., Doi M., Shimasaku K., Schneider D. P., 1996, *AJ*, **111**, 1748
- Gal R. R., 2008, *Optical Detection of Clusters of Galaxies*. Springer Netherlands, Dordrecht, pp 119–142. doi:10.1007/978-1-4020-6941-3\_4, [https://doi.org/10.1007/978-1-4020-6941-3\\_4](https://doi.org/10.1007/978-1-4020-6941-3_4)
- Gal R. R., de Carvalho R. R., Odewahn S. C., Djorgovski S. G., Margoniner V. E., 2000, *AJ*, **119**, 12
- Gal R. R., de Carvalho R. R., Lopes P. A. A., Djorgovski S. G., Brunner R. J., Mahabal A., Odewahn S. C., 2003, *AJ*, **125**, 2064
- Geach J. E., Murphy D. N. A., Bower R. G., 2011, *MNRAS*, **413**, 3059
- Gonzalez A., 2014, in *Building the Euclid Cluster Survey - Scientific Program*, proceedings of a conference held July 6-11 2014 at the Sixten Center for Astrophysics. p. 7
- Hashimoto T., Goto T., Momose R., Ho C.-C., Makiya R., Chiang C.-Y., Kim S. J., 2019, *MNRAS*, **489**, 2014
- Henriques B. M. B., White S. D. M., Thomas P. A., Angulo R., Guo Q., Lemson G., Springel V., Overzier R., 2015, *MNRAS*, **451**, 2663
- Hilton M., et al., 2021, *ApJS*, **253**, 3
- Jiménez-Teja Y., Vílchez J. M., Dupke R. A., Lopes P. A. A., de Oliveira N. O. L., Coe D., 2021, arXiv e-prints, p. arXiv:2109.04485
- Katgert P., et al., 1996, *A&A*, **310**, 8
- Kepner J., Fan X., Bahcall N., Gunn J., Lupton R., Xu G., 1999, *The Astrophysical Journal*, **517**, 78
- Kim R. S. J., et al., 2002, *AJ*, **123**, 20
- Kitzbichler M. G., White S. D. M., 2007, *MNRAS*, **376**, 2
- Koester B. P., et al., 2007, *ApJ*, **660**, 239
- Kravtsov A. V., Borgani S., 2012, *ARA&A*, **50**, 353
- Lidman C. E., Peterson B. A., 1996, *AJ*, **112**, 2454
- Lopes P. A. A., 2007, *MNRAS*, **380**, 1608
- Lopes P. A. A., Ribeiro A. L. B., 2020, *MNRAS*, **493**, 3429
- Lopes P. A. A., de Carvalho R. R., Gal R. R., Djorgovski S. G., Odewahn S. C., Mahabal A. A., Brunner R. J., 2004, *AJ*, **128**, 1017
- Lopes P. A. A., de Carvalho R. R., Kohl-Moreira J. L., Jones C., 2009, *MNRAS*, **392**, 135
- Lopes P. A. A., Ribeiro A. L. B., Rembold S. B., 2014, *MNRAS*, **437**, 2430
- Maraston C., 2005, *MNRAS*, **362**, 799
- Markevitch M., Gonzalez A. H., Clowe D., Vikhlinin A., Forman W., Jones C., Murray S., Tucker W., 2004, *ApJ*, **606**, 819
- McNamara B. R., Nulsen P. E. J., 2007, *ARA&A*, **45**, 117
- Mehrtens N., et al., 2012, *MNRAS*, **423**, 1024
- Mendes de Oliveira C. L., Cypriano E. S., Sodré Laerte J., 2006, *AJ*, **131**, 158
- Mendes de Oliveira C., et al., 2019, *Monthly Notices of the Royal Astronomical Society*, p. 2048
- Merson A. I., et al., 2013, *MNRAS*, **429**, 556
- Merten J., et al., 2011, *MNRAS*, **417**, 333
- Merten J., et al., 2015, *ApJ*, **806**, 4
- Milkeraitis M., Waerbeke L. V., Heymans C., Hildebrandt H., Dietrich J. P., Erben T., 2010, *Monthly Notices of the Royal Astronomical Society*, **406**, 673
- Molino A., et al., 2020, *MNRAS*, **499**, 3884
- Monteiro-Oliveira R., Cypriano E. S., Machado R. E. G., Lima Neto G. B., Ribeiro A. L. B., Sodré L., Dupke R., 2017, *MNRAS*, **466**, 2614

- Nakazono L., et al., 2021, [Monthly Notices of the Royal Astronomical Society](#), 507, 5847–5868
- Okabe N., Smith G. P., Umetsu K., Takada M., Futamase T., 2013, [ApJ](#), 769, L35
- Peng Y.-j., et al., 2010, [ApJ](#), 721, 193
- Pierpaoli E., Borgani S., Scott D., White M., 2003, [MNRAS](#), 342, 163
- Planck Collaboration et al., 2014, [A&A](#), 571, A16
- Poggianti B. M., Smail I., Dressler A., Couch W. J., Barger A. J., Butcher H., Ellis R. S., Oemler Augustus J., 1999, [ApJ](#), 518, 576
- Postman M., Lubin L. M., Gunn J. E., Oke J. B., Hoessel J. G., Schneider D. P., Christensen J. A., 1996, [AJ](#), 111, 615
- Puddu E., et al., 2021, [A&A](#), 645, A9
- Ramella M., Boschin W., Fadda D., Nonino M., 2001, [A&A](#), 368, 776
- Ramella M., Geller M. J., Pisani A., da Costa L. N., 2002, [AJ](#), 123, 2976
- Rykoff E. S., et al., 2014, [ApJ](#), 785, 104
- Rykoff E. S., et al., 2016, [The Astrophysical Journal Supplement Series](#), 224, 1
- Shamshiri S., Thomas P. A., Henriques B. M., Tojeiro R., Lemson G., Oliver S. J., Wilkins S., 2015, [MNRAS](#), 451, 2681
- Springel V., et al., 2005, [Nature](#), 435, 629
- Takey A., Durret F., Mahmoud E., Ali G. B., 2016, [A&A](#), 594, A32
- Takey A., Durret F., Márquez I., Ellien A., Molham M., Plat A., 2019, [MNRAS](#), 486, 4863
- Tempel E., Tuvikene T., Kipper R., Libeskind N. I., 2017, [A&A](#), 602, A100
- Wen Z. L., Han J. L., 2015, [ApJ](#), 807, 178
- Wetzel A. R., Tinker J. L., Conroy C., van den Bosch F. C., 2013, [MNRAS](#), 432, 336
- van Breukelen C., Clewley L., 2009, [MNRAS](#), 395, 1845

## APPENDIX A: TABLES

We provide a catalogue of galaxy clusters with  $S/N > 3.3$  in Table 2, the columns are described in Table A1. This table includes the catalogues the clusters were previous found and the new clusters. We do a further analysis for  $S/N > 5.0$  clusters, we provide sizes, masses and number of members. The galaxy member candidates are included in Table A2.

**Table A1.** Galaxy clusters and groups catalogue columns.

Column	Description
ID1	S-PLUS ID
ID2	PzWav ID
RA (deg)	Right Ascension in degrees
DEC (deg)	Declination in degrees
z	Cluster redshift
zerr	Cluster redshift error
znew	Redshift considering spectroscopic data
znewerr	Spectroscopic redshift error
Nmemb	Number of members
SN	Signal-to-noise richness
rich	PzWav richness
rich2	Membership analysis richness
rich2err	Membership analysis richness error
radius	Radius from PzWav in Mpc
r200	R <sub>200</sub> using spectroscopic analysis in Mpc
r200err	R <sub>200</sub> error using spectroscopic analysis in Mpc
r200 <sub>2</sub>	R <sub>200</sub> from a scaling relation between richness and r200 in Mpc
r200 <sub>2lo</sub>	r200 <sub>2</sub> lower value in Mpc
r200 <sub>2hi</sub>	r200 <sub>2</sub> higher value in Mpc
m200	M <sub>200</sub> in 10 <sup>14</sup> M <sub>⊙</sub>
M200 <sub>lo</sub>	m200 lower value in 10 <sup>14</sup> M <sub>⊙</sub>
M200 <sub>hi</sub>	m200 higher value in 10 <sup>14</sup> M <sub>⊙</sub>
vdisp	Velocity dispersion in km/s
vdisp <sub>lo</sub>	Velocity dispersion lower value in km/s
vdisp <sub>hi</sub>	Velocity dispersion higher value in km/s
isnew	If 1 the cluster is new, 0 if not
cat	Catalogues the cluster was detected

**Table A2.** Table with galaxy membership for clusters with  $S/N > 5.0$ . The full table has additional columns with magnitudes in different filters and other information about the galaxies. Details about the columns are in Table A3.

RA	DEC	uJAV	J078	J095	J0410	J0430	gSDSS	J0515	rSDSS	J0660	iSDSS	J0861	rSDSS	rad	radmpc	LOG10(SIGMA, 5)	SIGMA(gals/Mpc <sup>2</sup> )	Mg	Mr	(g,r)	Radius	rphot	rphot_err	Delts_z	prob_gal	R200	rspec_z/r	zcls	SN	flag	probm	probh	DRG_ID
53.531164	-1.264016	19.906	20.802	-	20.06	18.99	18.65	17.76	17.61	17.240	18.88	16.76	0.010	0.09670	0.06635	4.85685	-20.838	-21.64	0.805	0.20340	0.158	0.0110	0.0022	1.00	0.490	0.155	13	30.937	0	0.868880	0.113120	77.0076	
53.538419	-1.268757	20.189	20.935	20.058	20.54	19.63	19.26	18.94	18.69	18.30	18.300	18.26	18.12	0.019	0.18250	0.43709	2.73586	-20.496	-20.81	0.316	0.37250	0.176	0.0210	0.0182	1.00	0.490	0.155	13	30.937	0	0.741909	0.258091	77.0078
53.538371	-1.256386	21.027	20.684	20.345	20.41	19.67	19.20	18.78	18.17	18.00	17.680	17.38	17.25	0.022	0.21040	0.46902	2.94453	-19.974	-20.82	0.848	0.42932	0.141	0.0140	-0.0126	1.00	0.490	0.155	13	30.937	0	0.853306	0.146694	77.0068
53.537328	-1.249010	21.114	21.803	21.007	21.17	20.88	19.99	19.44	18.90	18.74	18.500	18.15	18.09	0.039	0.37560	0.38217	2.41086	-19.478	-20.22	0.737	0.77036	0.141	0.0130	-0.0126	0.999	0.490	0.155	13	30.937	0	0.726330	0.273670	77.0063
53.537324	-1.243113	21.199	20.998	20.391	-	20.06	19.59	19.34	18.87	18.81	18.410	18.32	18.16	0.048	0.46700	-1.53682	0.02905	-17.969	-18.63	0.656	0.95315	0.071	0.0260	-0.0727	0.999	0.490	0.155	13	30.937	1	0.239796	0.760204	77.0053
53.510563	-1.236788	21.269	20.454	20.102	20.69	19.28	18.77	18.43	17.89	17.72	17.390	17.11	17.11	0.031	0.30720	0.71982	5.24593	-20.286	-21.00	0.714	0.61873	0.134	0.0130	-0.0182	1.00	0.490	0.155	13	30.937	0	0.609907	0.306993	77.0096
53.545752	-1.218556	21.504	21.864	-	21.82	21.71	19.69	19.43	18.63	18.41	18.050	17.68	17.63	0.030	0.28710	0.64264	4.39181	-19.825	-20.52	0.697	0.66642	0.142	0.0150	-0.0117	0.999	0.490	0.155	13	30.937	0	0.869526	0.134974	77.0071
53.531424	-1.205958	21.655	21.056	21.685	20.18	20.15	19.91	19.26	18.70	17.94	18.160	17.85	17.83	0.025	0.24120	1.02596	10.61602	-19.638	-20.48	0.838	0.49226	0.143	0.0200	-0.0104	0.999	0.490	0.155	13	30.937	0	0.878324	0.121676	77.0087
55.365277	-1.224994	-	20.297	-	-	-	19.64	19.01	18.46	18.33	17.940	17.53	17.65	0.033	0.32410	0.38610	2.43273	-19.978	-20.78	0.799	0.66140	0.147	0.0170	-0.0074	1.00	0.490	0.155	13	30.937	0	0.881107	0.118893	77.0063
53.502313	-1.265431	20.173	20.318	19.853	19.82	19.13	18.92	18.76	18.11	18.01	17.690	17.56	17.44	0.003	0.03220	-1.40655	0.03922	-17.885	-18.59	0.708	0.10747	0.049	0.0120	-0.0854	0.97	0.300	0.147	17	30.568	1	0.301536	0.696464	79.0063



**Table A3.** Table with all columns and respective descriptions of Table A2.

Column	Description
RA (deg)	Right Ascension in degrees
DEC (deg)	Declination in degrees
uJAVA	Apparent magnitude
J0378	Apparent magnitude
J0395	Apparent magnitude
J0410	Apparent magnitude
J0430	Apparent magnitude
gSDSS	Apparent magnitude
J0515	Apparent magnitude
rSDSS	Apparent magnitude
J0660	Apparent magnitude
iSDSS	Apparent magnitude
J0861	Apparent magnitude
zSDSS	Apparent magnitude
zspec	Spectroscopic redshift
zspec-err	Spectroscopic redshift error
velocity	Velocity in km/s
velocity-err	Velocity error in km/s
R	Radial offset in degrees
Rmpc	Radial offset in Mpc
Velocity offset	Velocity relative to the cluster central velocity in km/s
Flagm	Spectroscopic classification in which: 0 = member and 1 = interloper
LOG10(SIGMA_5)	Log10 of density
SIGMA_5	Local galaxy density in $gals/Mpc^2$
Mg	Absolute magnitude
Mr	Absolute magnitude
(g-r)_0	Rest-frame color
Radius/R200	Distance to the cluster center normalized by R200
Velocity offset/VDISP	Velocity offset normalized by the velocity dispersion of the cluster
zphot	Photometric redshift
zphot_err	Photometric redshift error
Delta_z	$(z_{phot} - z_{spec_{cls}})/(1 + z_{spec_{cls}})$
Nmemb-200	Number of spectroscopic members within R200
R500	Physical radius of the cluster to which the galaxy belong in Mpc
R200	Physical radius of the cluster to which the galaxy belong in Mpc
M200	Mass of the cluster to which the galaxy belong in $10^{14} M_{\odot}$
Vdisp	Velocity dispersion of the cluster to which the galaxy belong in km/s
zspec_cls	Cluster spectroscopic redshift
cluster-index	Cluster ID
SN	Signal-to-noise
iflag	Photometric classification in which: 0 is a member and 1 is an intruder
probm	Probability of being member
probi	Probability of being intruder
iDR3_ID	Galaxy ID